^{57}Fe Hyperfine Coupling Tensors of the FeMo Cluster in *Azotobacter vinelandii* MoFe Protein: Determination by Polycrystalline ENDOR Spectroscopy

Anne E. True,[1a] Mark J. Nelson,[1b] Ronald A. Venters,[1c] William H. Orme-Johnson,*[1d] and Brian M. Hoffman*[1a]

Contribution from the Department of Chemistry, Northwestern University, Evanston, Illinois 60201, and Department of Chemistry, Massachusetts Institute of Technology, Cambridge, Massachusetts 02139. *Received June 12, 1987*

Abstract: ^{57}Fe ENDOR spectra obtained from frozen-solution samples of *Azotobacter vinelandii* molybdenum–iron protein (Av1) have been interpreted through use of a method we have devised for analyzing and simulating the ENDOR spectra of a randomly oriented polycrystalline (powder) paramagnet that has **g** and hyperfine tensors of arbitrary symmetry and relative orientation. The hyperfine tensor principal values *and* orientation relative to the **g** tensor (zero-field splitting tensor) have been determined for five distinct iron sites of the Av1 FeMo-cofactor cluster by examining the variations in the spectrum as the observing *g* value (static field) is moved across the EPR envelope. Along with the recent description of the molybdenum site of the cofactor, this brings to six the number of individual metal sites of the protein-bound FeMo-co cluster whose magnetic properties have been described by the ENDOR technique. The protein-bound cofactor cluster has a remarkably complex structure: No two of the five resolved Fe sites have equivalent hyperfine tensor components or orientation. The results are used to discuss the cluster's composition, the degree of intrinsic versus protein-imposed structural complexity, and the Fe-site properties.

The molybdenum–iron (MoFe) protein of nitrogenase is an $\alpha_2\beta_2$ dimer that contains 2 Mo, 30 (±3) Fe, and approximately 30 labile S atoms.[2] Mössbauer and EPR measurements indicate that these inorganic components are organized in a minimum of six polynuclear metal clusters,[2,3] with the molybdenum–iron cofactor (FeMo-co) cluster of approximate composition $MoFe_{6-8}S_{9\pm1}$,[4] representing two of these. The structure of this EPR-active cluster is unknown and is the subject of intensive investigation because of convincing evidence that it is a constituent of the active site of nitrogenase.[5]

As part of this effort we reported the use of isotopically enriched proteins to obtain electron nuclear double resonance (ENDOR) signals from *each* type of atom known to be associated with the cofactor, ^{1}H, ^{57}Fe, ^{95}Mo, and ^{33}S, and to compare MoFe proteins, Av1, Kp1, and Cp1,[6] isolated, respectively, from the three organisms *Azotobacter vinelandii*, *Klebsiella pneumoniae*, and *Clostridium pasteurianum*.[7,8] This study yielded hyperfine and quadrupole coupling constants for the molybdenum site of the cofactor that are interpretable in terms of an unsymmetrically coordinated Mo^{IV} ion. Selected, single-crystal-like,[9] ^{57}Fe spectra were obtained from at least five distinct iron sites in each of the three enzymes,[10] and a partial analysis indicated each to have a distinct set of magnetic, and thus chemical, characteristics. However, this work did not attempt to deduce in full the hyperfine tensor principal values and relative orientations of each individual iron site. As such, it did not fully address the level of equivalence among sites and did not permit us to discuss the valency formalisms applicable to those sites, nor did it resolve the question of the number of sites detectable in ENDOR measurements at X-band.

This report presents a full set of ^{57}Fe ENDOR spectra obtained from frozen-solution samples of Av1. The measurements have been interpreted through use of a method devised for analyzing and simulating the ENDOR spectra of a randomly oriented polycrystalline (powder) paramagnet that has **g** and hyperfine tensors of arbitrary symmetry and relative orientation.[11] The theory was developed to permit us to determine the principal values of a hyperfine tensor *and* the orientation relative to the **g** tensor (zero-field splitting tensor) by examining the variations in the spectrum as the observing *g* value (static field) is moved across the EPR envelope, and it already has been applied to the analysis of ^{14}N and ^{57}Fe ENDOR data taken from sulfite reductase[12] and ^{17}O ENDOR data taken in studies of aconitase.[13] Its present application, however, is without precedent: We have fully characterized the magnetic hyperfine tensors of *five* distinct iron sites of the Av1 cofactor cluster, which must have a remarkably complex structure, since no two are equivalent. Along with the recent description of the molybdenum site of the cofactor, this brings to six the number of individual metal sites of the protein-bound FeMo-co cluster whose magnetic properties have been characterized by this technique.

Experimental Procedures

Natural-abundance and ^{57}Fe-enriched samples of nitrogenase from *A. vinelandii* were prepared as described elsewhere.[8] EPR and ENDOR measurements were obtained in a modified Varian Associates E-109 EPR

---

[1] (a) Northwestern University. (b) Massachusetts Institute of Technology. Current address: Experimental Station, E. I. du Pont de Nemours & Co., Wilmington, DE 19898. (c) Northwestern University. Current address: Duke University Medical Center, Durham, NC 27710. (d) Massachusetts Institute of Technology.

[2] (a) Orme-Johnson, W. H. *Annu. Rev. Biophys. Chem.* **1985**, *14*, 419–459. (b) Nelson, M. J.; Lindahl, P. A.; Orme-Johnson, W. H. *Adv. Inorg. Biochem.* **1982**, *4*, 1–40. (c) Mortenson, L. E.; Thorneley, R. N. F. *Annu. Rev. Biochem.* **1979**, *48*, 387–418. (d) Brill, W. J. *Microbiol. Rev.* **1980**, *44*, 449–467.

[3] (a) Zimmerman, R.; Munck, E.; Brill, W. J.; Shah, V. K.; Henzl, M. T.; Rawlings, J.; Orme-Johnson, W. H. *Biochim. Biophys. Acta* **1978**, *537*, 185–207. (b) Huynh, B. H.; Munck, E.; Orme-Johnson, W. H. *Biochim. Biophys. Acta* **1979**, *576*, 192–203. (c) Huynh, B. H.; Henzl, M. T.; Christner, J. A.; Zimmermann, R.; Orme-Johnson, W. H.; Munck, E. *Biochim. Biophys. Act* **1980**, *623*, 124–138.

[4] Nelson, M. J.; Levy, M. A.; Orme-Johnson, W. H. *Proc. Natl. Acad. Sci., U.S.A.* **1983**, *80*, 147–150.

[5] Hawkes, T. R.; McLean, P. A.; Smith, B. E. *Biochem. J.* **1984**, *217*, 317–321.

[6] The following abbreviations are used: Av1, Kp1, and Cp1, the molybdenum–iron proteins, respectively, from *A. vinelandii*, *K. pneumoniae*, and *C. pasteurianum*; MoFe, molybdenum–iron protein; FeMo-co, molybdenum–iron cofactor; ENDOR, electron nuclear double resonance.

[7] (a) Hoffman, B. M.; Roberts, J. E.; Orme-Johnson, W. H. *J. Am. Chem. Soc.* **1982**, *104*, 860–862. (b) Hoffman, B. M.; Venters, R. A.; Roberts, J. E.; Nelson, M. J.; Orme-Johnson, W. H. *J. Am. Chem. Soc.* **1982**, *104*, 4711–4712.

[8] Venters, R. A.; Nelson, M. J.; McLean, P. A.; True, A. E.; Levy, M. A.; Hoffman, B. M.; Orme-Johnson, W. H. *J. Am. Chem. Soc.* **1986**, *108*, 3487–3498.

[9] Rist, G. H.; Hyde, J. S. *J. Chem. Phys.* **1970**, *52*, 4633–4643.

[10] A preliminary analysis of the ^{57}Fe ENDOR measurements was interpreted in terms of six distinct iron sites.[7b] This was corrected to five distinct sites in ref 8.

[11] (a) Hoffman, B. M.; Martinsen, J.; Venters, R. A. *J. Magn. Reson.* **1984**, *59*, 110–123. (b) Hoffman, B. M.; Venters, R. A.; Martinsen, J. *J. Magn. Reson.* **1985**, *62*, 537–542.

[12] (a) Cline, J. F.; Janick, P. A.; Siegel, L. M.; Hoffman, B. M. *Biochemistry* **1985**, *24*, 7942–7947. (b) Cline, J. F.; Janick, P. A.; Siegel, L. M.; Hoffman, B. M. *Biochemistry* **1986**, *25*, 4647–4654.

[13] Telser, J.; Emptage, M. H.; Merkle, H.; Kennedy, M. C.; Beinert, H.; Hoffman, B. M. *J. Biol. Chem.* **1986**, *261*, 4840–4846.

0002-7863/88/1510-1935$01.50/0

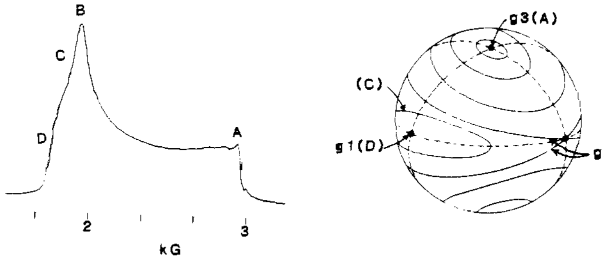

Figure 1. Correspondences between magnetic field values in an EPR spectrum and field orientations within the molecular *g* frame. Left: EPR absorption envelope for the Av1 protein. Spectrum is a dispersion derivative taken with 100-kHz field modulation at 2 K under conditions of rapid adiabatic passage. Right: Unit sphere with curves of constant *g* factor drawn and several correspondences indicated.

spectrometer previously described in detail.[8]

EPR and ENDOR Analyses

EPR Spectra. The EPR signal of the MoFe protein arises from the $S = {}^3/_2$ spin state of the cofactor cluster (Figure 1).[2,3] The spin Hamiltonian for this state of the cluster includes terms for the fine structure and the interaction of the electronic spin with the external field[14] (eq 1). Here D and E are the axial and

$$\begin{aligned}\hat{H}_e &= \hat{H}_{zfs} + \hat{H}_z \\ &= [D(\hat{S}_z{}^2 - {}^5\!/_4) + E(\hat{S}_x{}^2 - \hat{S}_y{}^2)] + \beta\hat{S}\cdot\mathbf{g}\cdot B \end{aligned} \tag{1}$$

rhombic zero-field splitting parameters and the rhombicity is measured by $\lambda = E/D$. Typically, the $S = {}^3/_2$ **g** tensor is taken to be isotropic, but it is easy to further allow for an axial symmetry: $g_x = g_y = g_\perp$; $g_z = g_\parallel$.

In zero applied field the $S = {}^3/_2$ spin quartet is split into two Kramers' doublets, separated by the zero-field splitting energy, $\Delta = 2D(1 + 3\lambda^2)^{1/2}$; analysis of the ^{57}Fe ENDOR data gave $\Delta = 12.2$ cm^{-1} for Av1.[8] As this energy is large compared with k_BT at helium temperatures, as well as with the interaction with the external field, the EPR spectrum of Av1 is associated solely with the lower, m_s = "$\pm{}^1/_2$" doublet. As such it can be described in a representation based on a fictitious spin, $S' = {}^1/_2$. In this representation the spectrum is characterized by a **g**′ tensor that is coaxial with the fine-structure interaction[15] (eq 2). For Av1,

$$\hat{H}_{ze}' = \hat{S}'\cdot\mathbf{g}'\cdot B \tag{2a}$$

$$g_3' = g_\parallel$$

$$g_{2\text{or}1}' = g_\perp\left[1 + \frac{1 \mp 3|\lambda|}{(1 + 3\lambda^2)^{1/2}}\right] \tag{2b}$$

$g_1' = 4.32$, $g_2' = 3.68$, and $g_3' = 2.01$, which corresponds to $S = {}^3/_2$ representation parameters, $g_\parallel = 2.01$, $g_\perp = 2.005$, and $|\lambda| = 0.053$.[8]

When the protein is subjected to a magnetic field B whose direction within the molecular **g**′-tensor (fine-structure) reference frame is described by the polar and azimuthal angles (λ, ϕ), then the EPR resonance field for that orientation is described by the well-known expression[14] for the angle-dependent g' value, $h\nu = g'\beta B$, where

$$g'^2 = g'^2(\theta, \phi) = \tilde{l}\cdot\tilde{\mathbf{g}}'\cdot\mathbf{g}'\cdot l = \sum g_i'^2 l_i^2 \tag{3}$$

$B = \text{B}l$, and l is a unit vector parallel to B: $l = (\sin\theta\cos\phi, \sin\theta\sin\phi, \cos\theta) = (l_1, l_2, l_3)$. When ENDOR spectra of polycrystalline samples and their simulations are considered, the observing field is best denoted by the corresponding g' value. In discussing the experimental results below, we shall omit the primes on g' when no confusion can arise.

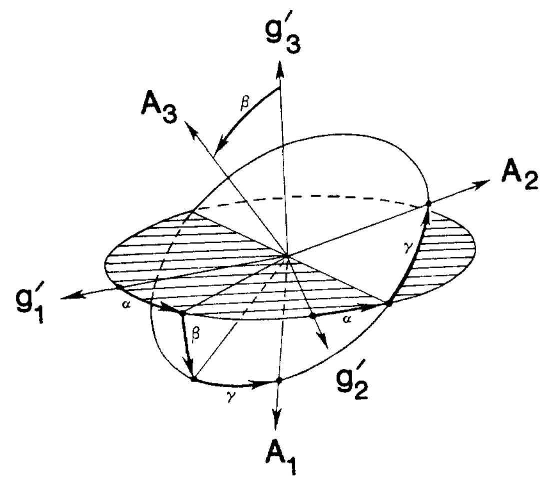

Figure 2. Definition of the Euler angles (α, β, γ) relating $S = {}^3/_2$ local (diagonal) nuclear hyperfine tensor axes to **g**′-tensor (zero-field splitting) axes.

ENDOR Frequencies. The interaction between the $S = {}^3/_2$ cluster electronic spin and the nuclear spin of an individual ^{57}Fe site within the cluster is included by adding a hyperfine interaction term to the Hamiltonian (eq 4).[14] The **A** for each ^{57}Fe site is

$$\hat{H}_{\text{hf,loc}} = h\hat{I}\cdot\mathbf{A}\cdot\hat{S} = h\hat{I}\cdot\begin{bmatrix} A_1 & & \\ & A_2 & \\ & & A_3 \end{bmatrix}\cdot\hat{S} \tag{4}$$

diagonal within its own local principal axis coordinate frame, and the orientation of that frame with respect to the g-tensor reference frame can be expressed in terms of the three Euler angles (α, β, γ) (Figure 2).[15] Because the ENDOR spectra of the individual iron sites are additive, each site can be treated separately; for clarity we normally suppress identifying superscripts. The first step to obtaining the ENDOR transition frequencies involves expressing the hyperfine interaction tensor in the g-tensor reference frame, using the rotation matrix, $\mathbf{M}(\alpha, \beta, \gamma)$:[15b]

$${}^g\mathbf{A} = \mathbf{M}^{-1}\cdot\mathbf{A}\cdot\mathbf{M} \tag{5}$$

This leads to a hyperfine Hamiltonian in the $S = {}^3/_2$ representation

$$\hat{H}_{\text{hf}} = h\hat{I}\cdot{}^g\mathbf{A}\cdot\hat{S} = h\sum {}^gA_{ij}\hat{I}_i\hat{S}_j \tag{6}$$

Through use of the Wigner–Eckart theorem,[14] this can be transformed to the effective-spin ($S' = {}^1/_2$) representation

$$\hat{H}_{\text{hf}} = \text{h}\hat{I}\cdot\mathbf{A}'\cdot\hat{S}' \qquad A_{ij} = {}^gA_{ij}g_j'/g_j \tag{7a}$$

and can be written in matrix form:

$$\mathbf{A}' = {}^g\mathbf{A}\cdot\bar{g}' \qquad \bar{g}'_{ij} = \delta_{ij}g_j'/g_j \tag{7b}$$

The $S = {}^3/_2$ g values for Av1 deviate negligibly from $g = 2.0$, and for all but the most exacting work, this may be expressed in terms of the **g**′ tensor

$$\mathbf{A}' = {}^g\mathbf{A}\cdot\mathbf{g}'/2 \qquad g'_{ij} = \delta_{ij}g_j' \tag{7c}$$

The final term needed to describe an ENDOR measurement of an $I = {}^1/_2$ nucleus is the nuclear Zeeman interaction. In most cases this can be taken as a scalar coupling, $\hat{H}_{nz} = \beta_n g_N \hat{I}\cdot B$, and is characterized by a nuclear Larmor frequency, $\nu_N{}^0 = g_N\beta_n\text{B}$, where g_N is the g factor for the free nucleus. However, the m_s = "$\pm{}^3/_2$" electronic spin doublet that arises from the zero-field splitting of the total spin $S = {}^3/_2$ ground state of the MoFe protein provides a low-lying electronic state that gives rise to a large, anisotropic pseudonuclear Zeeman effect.[14] Because of this, the nuclear Zeeman interaction is determined by an effective nuclear $\mathbf{g}^N$ tensor that is coaxial with the zero-field splitting tensor, and thus the g tensor. We find that in the general case of noncoaxial hyperfine and g tensors, this takes the form (for $S = {}^3/_2$) shown in eq 8. Note that there is no contribution of the pseudonuclear

---

[14] Abragam, A.; Bleaney, B. *Electron Paramagnetic Resonance of Transition Ions*; Clarendon: Oxford, 1970.

[15] (a) We choose to work in a right-handed coordinate system in which $g_1' > g_2' > g_3'$. This is identical with that of the fine-structure Hamiltonian (eq 1) for $\lambda < 0$ with the axes corresponding as $(x, y, z) \leftrightarrow (1, 2, 3)$. If the convention $\lambda > 0$ is adopted, then our working coordinate system is related to that of eq 1 by a 90° rotation about the z axis. (b) Our treatment of coordination transformations follows: Mathews, J.; Walker, R. L. *Mathematical Methods of Physics*; W. A. Benjamin: New York, 1965.

$$\hat{H}_{\mathrm{nz}} = \beta_n \hat{I} \cdot \mathbf{g}_{\mathrm{N}} \cdot B \tag{8}$$

$$g_{ij}{}^{\mathrm{N}} = g_{\mathrm{N}}[\delta_{ij} + {}^{3}\!/_{2}(g_e\beta/g_{\mathrm{N}}\beta_n)({}^{g}A_{ij}/\Delta)(1 - \delta_{j3})]$$

Zeeman effect to interactions with the $z(g_3')$ component of the external field. For nuclei with small g_{N}, such as ^{57}Fe ($g_{\mathrm{Fe}} = 0.18$), the effect can be large and, depending on the magnitude of ${}^{g}A_{ij}/\Delta$ and the sign of ${}^{g}A_{ij}$, ν_{N} may range from $\nu_{\mathrm{N}} \gg \nu_{\mathrm{N}}{}^{0}$ through $\nu_{\mathrm{N}} \sim 0$, and even $\nu_{\mathrm{N}} < 0$, the latter corresponding merely to a reversal of the line positions. It was analysis of this effect that yielded the signs of the hyperfine couplings for the ^{57}Fe sites of the FeMo-co cluster of Av1, as well as the value of Δ quoted above.[8]

The transition frequencies measured in an ENDOR experiment are determined by the nuclear interaction terms, eq 7 and 8. To first order, these can be written[16] as in eq 9, where $V_{\pm}$ is the vector

$$\hat{H}_{\mathrm{int}} = h\hat{I} \cdot V_{\pm} \tag{9}$$

sum of the effective hyperfine and nuclear Zeeman fields (eq 10)

$$\begin{aligned} V_{\pm} &= \left[(\pm{}^{1}\!/_{2})\frac{1}{g}\mathbf{A}' \cdot \mathbf{g}' - \frac{\beta_n}{h} B \cdot \mathbf{g}^{\mathrm{N}} \right] \cdot l \\ &\equiv \mathbf{K}_{\pm} \cdot l \end{aligned} \tag{10}$$

and the subscript refers to the electronic quantum number $m_s' = \pm{}^{1}/_{2}$. Without regard to the relative magnitude of hyperfine and nuclear Zeeman terms, the first-order ENDOR transition frequencies are then given by eq 11.

$$\begin{gathered} \nu_{\pm} = K_{\pm} = [K_{\pm}{}^{2}]^{1/2} \\ K_{\pm}{}^{2} = \tilde{l} \cdot \tilde{\mathbf{K}}_{\pm} \cdot \mathbf{K}_{\pm} \cdot l \equiv \tilde{l} \cdot \mathbf{K}_{\pm}{}^{2} \cdot l \end{gathered} \tag{11}$$

It is useful to emphasize that the lower Kramers' doublet of an $S = {}^{3}/_{2}$ spin system with large zero-field splitting has a strongly anisotropic magnetic moment, which forces the effective hyperfine interaction tensor $\mathbf{A}'$ (eq 7) to be highly anisotropic. Even if the intrinsic site hyperfine interaction were isotropic, $A_1 = A_2 = A_3 = a$ (eq 4), by eq 7 the ENDOR frequencies for Av1 (eq 11) would be described by an anisotropic hyperfine tensor in the $S' = {}^{1}/_{2}$ representation (eq 12), with effective hyperfine couplings associated with g_1' and g_2' that are roughly double the intrinsic values,

$$\begin{gathered} A_1' = A\frac{g_1'}{g_{\perp}} \sim 2.15a \qquad A_2' = A\frac{g_2'}{g_{\perp}} \sim 1.8a \\ A_3' = A\frac{g_3'}{g_{\parallel}} \sim a \end{gathered} \tag{12}$$

as are any small differences between nearly equivalent ^{57}Fe sites. This doubling spreads out the ENDOR spectra taken at low observing fields, greatly enhances resolution, and ultimately is the reason why the measurements reported here have been possible.

Simulating Polycrystalline ENDOR Spectra. This section briefly presents the elements of the recently developed theory[11,17] and then the procedures for its application. The EPR spectrum of a frozen solution is a superposition of the resonances from the random distribution of all protein orientations. ENDOR spectra are taken with the external field fixed within the EPR envelope at a selected value B, which corresponds to a g value determined by the spectrometer frequency, $g = h\nu/\beta\mathrm{B}$. As recognized by Hyde and his co-workers,[9] ENDOR spectra taken with the magnetic field set at the extreme edges of the EPR spectrum of Av1 (positions A and D in Figure 1), near the maximal or minimal g values, give single-crystal-like patterns from the subset of molecules for which the magnetic field happens to be directed along a g-tensor axis. An ENDOR spectrum obtained by using an intermediate field and g value (e.g., C) does not arise from a single orientation, but rather from a well-defined subset of molecular orientations. When the existence of a finite component EPR line width (δ-function EPR envelope) is ignored, the EPR signal intensity at field B, and thus the ENDOR spectrum, arises from those selected molecular orientations associated with the curve on the unit sphere, s_g, comprised of points for which the orientation-dependent spectroscopic splitting factor (eq 3) satisfies the condition $g'(\theta, \phi) = g$.[11a] However, although g is constant along the curve s_g, the ENDOR frequencies $\nu_{\pm}(\theta, \phi)$ (eq 11) are not. Thus, the ENDOR intensity in a spectrum of an $I = {}^{1}/_{2}$ nucleus taken at g falls in a range of frequencies spanning the values of $\nu_{\pm}$ associated with the selected subset of orientations associated with s_g.

At any observing g value within the EPR envelope of a polycrystalline (frozen-solution) sample, the intensity of a superposition ENDOR spectrum at radiofrequency ν can be written as a sum of convolutions over the ENDOR frequencies (eq 11) that arise on the curve s_g[11b]

$$^{\delta}I(\nu, g) = \textstyle\sum_{\pm} \displaystyle\int_{s_g} L(\nu - \nu_{\pm})\, e(\nu_{\pm})\, \mathrm{d}s \tag{13}$$

$$= \textstyle\sum_{\pm} \displaystyle\int_{s_g} L(\nu - \nu_{\pm})\, e(\nu_{\pm}) \left[\frac{\partial s}{\partial \phi} \right]_g \mathrm{d}\phi \tag{13a}$$

where

$$(\mathrm{d}s)^2 = (\mathrm{d}\theta)^2 + \sin^2\theta(\mathrm{d}\phi)^2 \tag{14}$$

and $L(x)$ is an ENDOR line-shape function and $e(\nu)$ is the hyperfine enhancement factor.[14] For $I = {}^{1}/_{2}$, the nuclear transition observed is ($m_{\mathrm{I}} = +{}^{1}/_{2} \leftrightarrow m_{\mathrm{I}} = -{}^{1}/_{2}$) and the summation involves only the electron spin quantum number $m_s' = \pm{}^{1}/_{2}$ (eq 10 and 11); for $I > {}^{1}/_{2}$, quadrupole terms must be included and the sum extended over the additional nuclear transitions.

To simulate experimental ENDOR spectra, the restriction to a δ-function EPR pattern must be relaxed. The complete expression for the relative ENDOR intensity at frequency ν, for an applied field set to a value B, involves the convolution of $^{\delta}I(\nu, g)$, the EPR envelope function derived by Kneubühl,[18] $S(H)$, and a component EPR line-shape function, $R(x)$:[11b]

$$I(\nu, \mathrm{B}) = \int_{g_{\mathrm{min}}}^{g_{\mathrm{max}}} \mathrm{dB}' S(\mathrm{B}')\, {}^{\delta}I(\nu, g')\, R(\mathrm{B} - \mathrm{B}') \tag{15}$$

This expression has been implemented as a BASIC program. The component line-shape functions $L(x)$ and $R(x)$ were both taken as Gaussians and the line widths as isotropic. The hyperfine enhancement factor usually could be ignored ($e(\nu) = 1$; eq 13).

An example of the ENDOR spectra predicted for a polycrystalline sample is presented in Figure 3A. Simulations with eq 13 were performed for a $S' = {}^{1}/_{2}$ paramagnetic center that has the rhombic g tensor of Av1 and an $I = {}^{1}/_{2}$ site that has a rhombic hyperfine tensor with $A_1' > A_2' > A_3'$; the $S = {}^{3}/_{2}$ tensor components have been chosen as those that characterize site A^{1} of Av1 (vide infra), but the pseudonuclear Zeeman effect was ignored ($\Delta \rightarrow \infty$ in eq 8). Consider first the case of coaxial tensors. The single-crystal-like ENDOR spectrum at the low (high) field g_1 (g_3) edge of the EPR envelope is a doublet split by twice the effective nuclear Larmor frequency (eq 8) and centered approximately at $A_1'/2$ ($A_3'/2$) (eq 11; Figure 3A). For intermediate fields, the pattern shifts and spreads. If the field is set to a value where the maximum and minimum frequencies in an ENDOR pattern do not shift rapidly as g is varied, each of the edges of the pattern appears as a well-defined intensity maximum in the form of a Larmor doublet (when resolved), as seen at $g = 3.69$ in Figure 3A. However, if the observing g is in a range where the ENDOR frequencies vary rapidly with g, then the doublet at an edge can appear as "steps" in ENDOR intensity, rather than peaks, as seen at $g = 3.9$ in Figure 3A.

It is convenient to represent the overall ENDOR response of a particular site as in Figure 3B, where each feature in an ENDOR spectrum at a given g is represented as a point; for clarity in Figure 3B, a doublet is given a single point at the frequency corresponding

---

[16] Thuomas, K.-A.; Lund, A. *J. Magn. Reson.* **1975**, *18*, 12–21.

[17] Other workers who have made contributions to the simulation of polycrystalline ENDOR patterns include: (a) Dalton, L. R.; Kwiram, A. L. *J. Chem. Phys.* **1972**, *57*, 1132–1145. (b) O'Malley, P. J.; Babcock, G. T. *J. Chem. Phys.* **1984**, *80*, 3912–3913. (c) Hurst, G. C.; Henderson, T. A.; Kreilick, R. W. *J. Am. Chem. Soc.* **1985**, *107*, 7294–7299. (d) van Willigen, H.; Chandrashekar, T. K. *J. Am. Chem. Soc.* **1986**, *108*, 709–713. (e) Brok, M.; Babcock, G. T.; de Groot, A.; Hoff, A. J. *J. Magn. Reson.* **1986**, *70*, 368–378.

[18] Kneubühl, F. K. *J. Chem. Phys.* **1960**, *33*, 1074–1078.

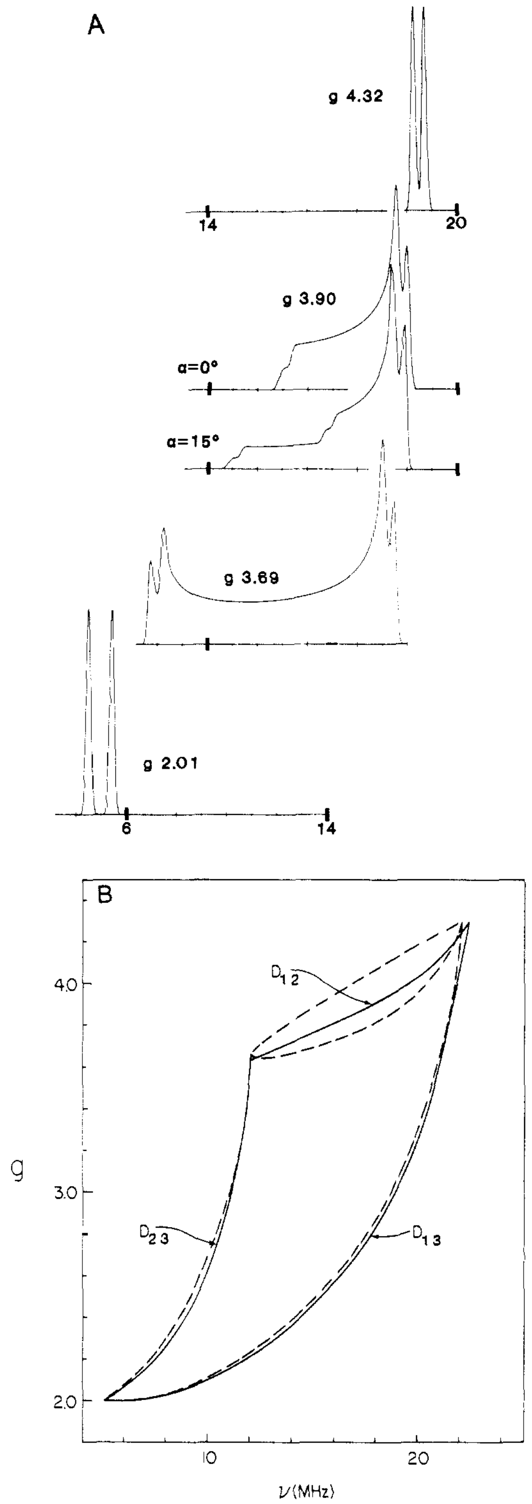

Figure 3. Calculated polycrystalline (superposition) ENDOR patterns versus observing g values for the rhombic **g** tensor of Av1 (4.32, 3.68, 2.01) and a ^{57}Fe ($I = {}^1/_2$) hyperfine tensor with principal values of site A^1 (−20.85, −13, −9.8) MHz. (A) Full spectra for selected g values as indicated; calculations employed eq 13 with a Gaussian shape, fwhm = 0.125 MHz, and for clarity the pseudonuclear Zeeman effect was ignored ($\Delta \rightarrow \infty$). All spectra have the same frequency scale; the top four are in registry, but the bottom spectrum has been offset as indicated. At g_1, g_2 and g_3 simulations with a rotation of the A tensor of $\alpha = 15°$ give simulations qualitatively similar to those with collinear tensors. However, for $g_1 > g > g_2$, there are sharp differences, as demonstrated when $g = 3.9$. (B) For a given observing g, the center frequency of the resolved features of calculated spectra such as those in (A) are given by the intersection(s) of a horizontal with the displayed curves. Collinear hyperfine and **g** tensors (—); noncollinear tensors, ($\alpha = 15°$, $\beta = \gamma = 0$) (- - -).

to its center. For the case represented in Figure 3, with $A_1' > A_2' > A_3'$, and still considering coaxial tensors, the higher frequency doublet, which we label D$_{13}$, moves smoothly between the frequencies associated with the two extremal, single-crystal-like fields at g_1 and g_3. The other, lower frequency doublet can best be labeled D$_{12}$ at fields such that $g_1' > g > g_2'$, and D$_{23}$ when $g_2' > g > g_3'$. It shifts to a center at $A_2/2$ as the field approaches g_2 either from above or below.

If the **g**′ and **A**′ tensors are not coaxial, then the ENDOR spectra and their field variation become more complex. For example, if the **A**′-tensor principal axis frame is rotated from the **g**′-tensor frame by a rotation about a single **g**′-tensor axis, say g_i', then the D$_{jk}$ doublet tends to split into two doublets for fields between g_j' and g_k'. In particular, for the case illustrated in Figure 3, a rotation about the g_3 axis splits the D$_{12}$-step doublet into two such steps in the low-field portion of the EPR spectrum, where $g_1' > g > g_2'$ (Figure 3). In coaxial cases where the edge displays a doublet of peaks, then upon rotation the edge is expected to split into two peak-doublets. Note also that when **g** and hyperfine tensors are not coaxial the hyperfine values measured at the edges of the EPR spectrum in general do not correspond to a principal axis value.

More complicated orientations of A' and g' frames, described by two or three Euler angles, can give correspondingly more complex patterns and field variations;[11] conversely, the set of spectra taken at multiple fields corresponds to a field-frequency pattern that is interpretable in terms of the relative orientation of **g**′ and **A**′ tensors, as well as of the principal values of the **A**′ tensors.

Analysis Procedure. The process of obtaining ^{57}Fe hyperfine tensor principal values and orientations begins with the accumulation and indexing of ENDOR spectra at multiple fields across the EPR envelope. Next, an initial approximation to the hyperfine principal values A_3 and A_1 is obtained from the ENDOR frequencies measured in the single-crystal-like spectra obtained, respectively, at the high- and low-field edges of the EPR envelope; A_2 is estimated from the spread of frequencies (when observable) in the spectrum taken at $g_{\mathrm{mid}} = g_2$. Then, the nature of the relative orientation of the **g** and **A** tensors is inferred from the development of the ENDOR pattern as the field increases from the low-field, g_1, edge of the EPR spectrum. In the present study, numerous trial and error simulations of selected spectra were then performed by varying the $S = {}^3/_2$ hyperfine interaction principal values and the relative orientation of **g**-tensor (fine-structure) and local nuclear-coordinate frames. These variations were constrained such that the parameters correctly predicted the resonance frequencies measured in the single-crystal-like spectra. In all cases, the analysis began with the simplest assumption, namely the minimal departure from coaxial **g** and **A** tensor, and was terminated when the entire accessible field-frequency range of ENDOR features had been accommodated.

In all but the ultimate simulations, the ENDOR line widths were optimized (eq 13) and the possible influence of a finite component EPR line width ignored. The final step was to increase the EPR line width until this had visible effect and then to see whether differential broadening altered the positions of the features or the shape of the pattern. This was not observed with any of the ^{57}Fe sites.

^{57}Fe ENDOR Measurements. With the field set to the high-field, $g_3 = 2$, edge of the EPR spectrum of ^{57}Fe-enriched Av1, the single-crystal-like ^{57}Fe ENDOR spectrum exhibits five resolved ^{57}Fe doublets (Figure 4A), thereby directly demonstrating that the cluster comprises at least five distinguishable iron sites.[8] The doublets form two groups, a lower frequency trio of resolved doublets centered at $A_3'/2 \sim 5$–6 MHz and a group of lines centered at $A_3'/2 \sim 10$ MHz consisting of at least two resolved doublets. Since there is no pseudonuclear Zeeman effect at g_3 (eq 8), the doublet splittings are simply $2\nu_{\mathrm{Fe}}{}^0$ and they do not signify the sign of A_{Fe}.

With the field set to give a single-crystal-like ENDOR spectrum at the low-field, g_1, edge of the EPR envelope, the ^{57}Fe pattern has six well-resolved peaks and is quite different from that at g

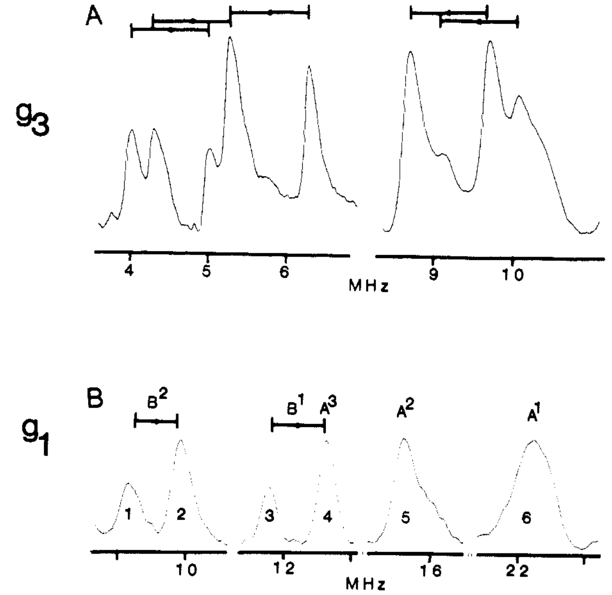

Figure 4. Single-crystal-like ^{57}Fe ENDOR spectra of the Av1 protein at (A) the high-field, g_3', edge of the EPR envelope and (B) the low-field, g_1' edge. The assignment of peaks to individual sites is indicated. (A) B = 3355 G, T = 2 K; microwave power, 0.63 mW; 100-kHz field modulation, 4 G; rf power, 30 W; rf scan rate, 3.5 MHz/s, 2000 scans. (B) Same as in A but B = 1572 G; 5000 scans; 1 MHz/division.

= 2 (Figure 4).[7b,8] For ^{57}Fe (g_{Fe} = 0.18) the effective nuclear Zeeman splitting at this field (eq 8) may be written in mixed, but convenient units, as eq 16, where $2\nu_{Fe}{}^0$ = 0.433 MHz at 1575 G,

$$2\nu_{Fe} = [1 + 1.02A_1\ (\mathrm{MHz})/\Delta\ (\mathrm{cm}^{-1})]2\nu_{Fe}{}^0 \qquad (16)$$

and for clarity only, coaxial **g** and **A** tensors have been assumed here. This simplified form of eq 8 demonstrates that the effective nuclear Zeeman splitting can differ drastically from $2\nu_{Fe}{}^0$. Because of this difference, an ENDOR measurement of $|A_1|$ and ν_{Fe} gives Δ to high precision as well as the sign of the ^{57}Fe hyperfine couplings. Through the use of eq 16 (or 8), the six peaks in Figure 4B were assigned as resonances from four distinct iron sites.[8] Peaks 1–4, located at lower frequency, comprise two doublets. They correspond to two sites, B^2 and B^1, that have small positive hyperfine coupling and enhanced nuclear Zeeman splittings; peaks 6 and 5 at higher frequency correspond, respectively, to sites A^1 and A^2, with larger, negative hyperfine couplings that lead (eq 8, 16) to a vanishingly small nuclear Zeeman splitting. The results presented below confirm the earlier suggestion[8] that peak 4 also derives intensity from an additional distinct site, A^3, with negative hyperfine coupling.

In addition to the single-crystal-like ^{57}Fe ENDOR spectra taken at the extreme edges of the EPR envelope, well-resolved ENDOR spectra have been taken at 25-G intervals ($\Delta g \sim 0.06$) as the field was increased from g_1 = 4.32 to g = 3.5. ENDOR spectra obtained upon further increasing the field from g = 3.5 to g = g_3 were poorly resolved because the peaks overlap, and thus spectra were taken only at 100-G intervals.

The analysis procedure described above is best applied if the evolution of the ^{57}Fe ENDOR pattern of an individual iron site can be traced as the field increases across the EPR envelope. In general, for Av1 the ^{57}Fe ENDOR peaks can be assigned for fields between $g = g_1$ = 4.3 and roughly $g \simeq 3.5$; poorer resolution at higher field precluded the direct experimental assignment of correspondences with the resonances at g_3. Since there is no pseudonuclear Zeeman effect at g_3, it was not possible even to determine which hyperfine interactions observed at this field are negative and which are positive.[19] This difficulty was addressed as follows. In three cases (sites A^2, A^3, B^1; see below) the correspondence could be made by observing the effects an assignment had on simulation of spectra taken at lower fields, $g \gtrsim 3.4$. The task was simplified because the choice of assignments is effectively binary: Since the five g_3 doublets fall into a low-frequency group of three sites and a higher frequency group of two sites, we had only to decide from simulations whether $A_3' \approx$ 10 or 20 MHz.

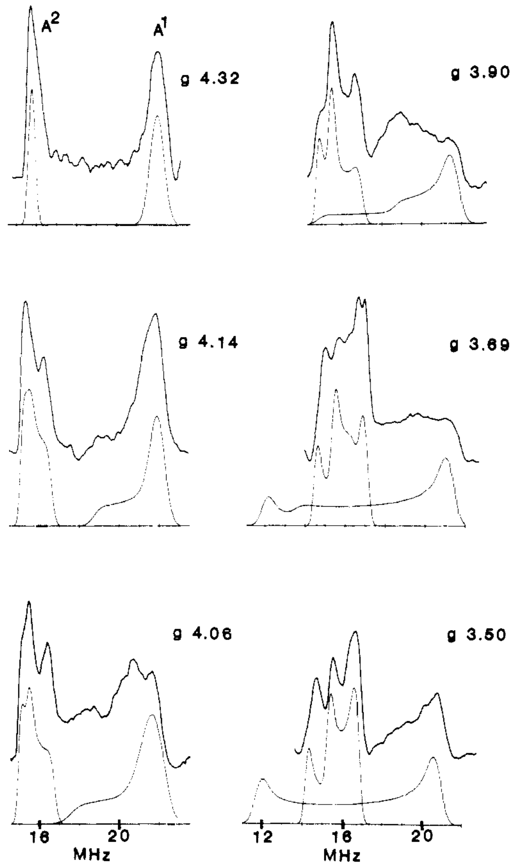

Figure 5. ^{57}Fe ENDOR spectra of iron sites A^1 and A^2 of the Av1 protein at selected magnetic fields. Computer simulations that employ the hyperfine interaction parameters of Table I are shown below the corresponding spectra; relative intensities for the two sites are set heuristically. Experimental conditions are the same as in Figure 4, with the g values as indicated. Each spectrum is the average of 1000 scans.

Sites A^1 and A^2. Figure 5 shows ENDOR spectra of iron sites A^1 and A^2 taken at various fields from g_1 to beyond g_2. Site A^1 has a negative hyperfine coupling and shows a single sharp peak at the low-field, g_1, edge of the EPR envelope (Figure 4B). The A^1 ENDOR pattern broadens rapidly to low frequency as the field is increased, which indicates that the hyperfine tensor is highly anisotropic, with $A_2 < A_1$ (Figure 5); accompanying this spread is a sharp reduction in intensity that makes detection unreliable by ca. g_2. The manner in which the pattern spreads as the field is increased from g_1 has been analyzed to obtain values for the tensor components and orientation (Table I) that generate simulations in satisfactory agreement with experiment (Figure 5). The parameters were obtained as follows.

Simulations of the A^1 pattern indicated that the observed spread to low frequency, for example, the breadth for $g \sim 4.14$, cannot be duplicated with coaxial **A** and **g** tensors, even by setting A_2 = 0 MHz. To match these observations requires that the local hyperfine tensor frame for site A^1 departs from the g-tensor frame by a rotation about the g_3 axis. Simulations were performed for various values of the angle α (Figure 2), and in each case an attempt was made to adjust A_2 and A_1 so that the calculated spectrum fit the low-frequency edge of the experimental data at g = 4.14 as well as the single-crystal peak at g = 4.32. As previously noted, when the **A** tensor is rotated about g_3, it is necessary to vary A_1 and A_2 jointly in order to reproduce the single-crystal pattern; for simplicity, we will mention only one of the coupled tensor components. (The same procedure is adopted below when discussing rotation by β about the g_2 axis.) The

---

[19] (a) Triple resonance experiments in principle could give these signs.[19b] To date, such efforts have been unsuccessful. (b) Kurreck, H.; Kirste, B.; White, W. *Angew. Chem., Int. Ed. Engl.* **1984**, *23*, 173–252.

Table I. ^{57}Fe Hyperfine Tensor Principal Values and Orientations Relative to Fine-Structure (g-Tensor) Principal Axes ($S = ^3/_2$ Representation) for Avl[a]

	A^1	A^2	A^3	B^1	B^2
		Principal Values, MHz			
A_1	−20.8	−14.0	−11.6	13.5	8.9
A_2	−13	−18.3	−14	11	11
A_3[b]	−10[c] (−19)	−19	−10	9	19[c] (10)
		Euler Angles,[d] deg			
α	15	10	30	0	12
β	0	15	0	45	0
R[e]	0.48 (0.62)	0.72	0.71	0.67	0.47 (0.80)

[a] For Avl the three principal values of the g′ tensor are 4.32, 3.68, 2.01. Uncertainties in the various hyperfine parameters are described in the Discussion. [b] The single-crystal-like spectra at g_3 display five doublets in two groups, three with $|A| \sim 10$ MHz (9.7, 9.8, 11.7 MHz) and two with $|A| \sim 19$ MHz (19.35, 19.5 MHz). Only assignments to, not within, a group are possible. (See text.) [c] By elimination, one of sites A^1 and B^2 must have $|A_3| \sim 10$ MHz and the other $|A_3| \sim 19$ MHz. The data reported here permit either assignment; the assignment tentatively preferred (without parentheses) is discussed in the text. [d] Euler angles as defined in Figure 2 and ref 11. In all cases, satisfactory fits were obtained with $\gamma = 0$. [e] R is defined as the ratio of the smallest to largest components of the A tensor.

spectrum at $g \sim 4.14$ could be fit by using a range of values ($\alpha \sim 10$–20°, $A_2 \sim 12$–14 MHz). Simulations with α much smaller or A_2 much larger did not reproduce the breadth of this pattern; a larger rotation moved the high-frequency edge outside the experimental pattern. An additional rotation of the A tensor by $\beta \leq 10°$ had no influence on the breadth of the pattern simulated. Within the acceptable (α; A_2) range for $g = 4.14$, further calculations showed that the reported values, $\alpha = 15°$, $A_2 = -13$ MHz, best reproduce the spectra at all fields. Simulations of the iron site A^1 with either $A_3 \sim -10$ MHz, as in Figure 5, or $A_3 \sim -20$ MHz were indistinguishable for the range of g values that gave resolved spectra ($g > 3.9$). Assignment of the A_3 values of other iron sites (see below) led us by elimination to the tentative assignment $A_3 = -10$ MHz for this site. No detectable distortion of the simulated ENDOR pattern was seen upon inclusion of EPR line widths up to 50 G for this or any other iron site, and as such the EPR line width was conveniently neglected.

The ^{57}Fe ENDOR pattern for site A^2 remains intense and does not spread very much as the field changes (Figure 5), which indicates a lesser anisotropy in the hyperfine tensor. The pattern, which starts as a single resonance centered at ~15.5 MHz at g_1, divides into three main peaks (Figure 5) that shift strongly as the observing field increases (Figures 5, 6). As confirmed by simulations, for all orientations sampled at low observing field $g > g_2$, the effective nuclear Zeeman splitting for this site is negligible ($2\nu_{\mathrm{Fe}} \sim 0$) because of the pseudonuclear effect, and the splittings are not due to this interaction. Simulations with collinear A and g tensors could not reproduce the breadth of the g_2 pattern no matter what value of A_2 was used, nor did these simulations exhibit more than two peaks. Simulations with a rotation of the hyperfine tensor around a single g-tensor axis, g_1 ($\alpha = 90$, $\beta \neq 0$, $\gamma = -90$), g_2 ($\beta \neq 0$), or g_3 ($\alpha \neq 0$), could reproduce the breadth of the pattern but generated only two peaks. Multiple rotations were needed to simulate the ENDOR pattern between g_1 and g_2, and the parameters were obtained as follows.

Simulations with $\alpha = 10°$, $|A_2| > |A_1|$, and $|A_2|$ chosen to correlate to the highest frequency peak at g_2 give a pattern that roughly matches the placement and breadth of the site A^2 pattern at fields between g_1 and g_2. However, such simulations do not give a resolved central feature. The breadth of the pattern was unchanged by introducing an additional rotation of the A tensor, $\beta \neq 0$, but the simulations now exhibited the necessary three peaks at g_2. Simulations with $\alpha = 10°$ and $\beta = 15°$ correlated well with the full set of experimental data. We assigned $A_3 \sim -20$ MHz for this site, rather than $A_3 \sim -10$ MHz, because any simulation that employed the latter value generated a pattern whose lowest frequency resonance is below any seen in the experimental spectra.

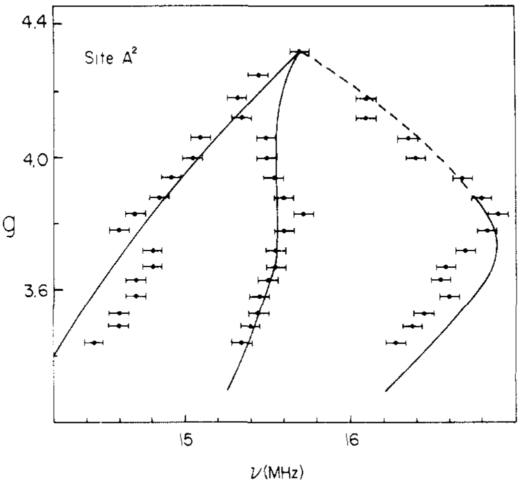

Figure 6. ENDOR peak positions versus observing g values for iron site A^2. The theoretical values, calculated by using the hyperfine tensor parameters given in Table I, are shown as solid lines for resolved peaks, dotted lines for features visible only as shoulders.

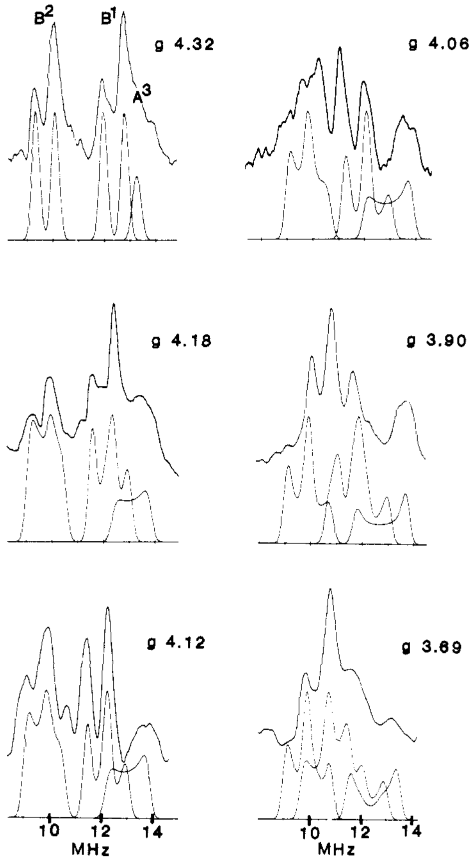

Figure 7. ^{57}Fe ENDOR spectra of iron sites A^3, B^1, and B^2 of the Avl protein at selected magnetic fields. The computer simulations, using hyperfine interaction parameters from Table I, are shown below the corresponding spectrum; relative intensities for the three sites are set heuristically. Experimental conditions are the same as in Figure 4 with the g values as indicated. Each spectrum is the average of 1000 scans.

Figure 5 shows that simulations based on the parameters listed in Table I reproduce the displayed experimental spectra quite well. Figure 6 shows in greater detail the agreement between the field dependence of the calculated and observed frequencies for the ENDOR peaks of site A^2.

Sites B^1, B^2, and A^3. Figure 7 shows the ENDOR spectra of iron sites B^1, B^2, and A^3 at various fields along the absorption envelope from g_1 up to and past g_2. Computer simulations using the final parameters for each site (Table I) are shown below each spectrum. Both sites B^1 and B^2 have positive hyperfine couplings and show a sharp single-crystal-like doublet at g_1 (Figure 4). Site

A^3 is not visible at this field. However, as the magnetic field is increased (Figure 7) a shoulder appears on peak 4, the high frequency partner peak of site B^1; by g_2, this shoulder has moved to higher frequency and is resolved into a peak that we call 4A. At fields greater than g_2, the peak retreats to lower frequency. In contrast to the behavior of peak 4A, the B^1 doublet (peaks 3 and 4) seen at g_1 moves sharply toward lower frequency as the magnetic field is increased (Figure 7); by g_2, the B^1 pattern merges with that of B^2. Numerous simulations that assumed the B^1 doublet and peak 4A together represent a single site and that employed the widest possible range of values for its hyperfine tensor orientation and principal components could not accommodate all the observations. In particular, a three-dimensional grid (5–10° intervals) in a space of the three Euler angles (α, β, γ) was explored over the range of physically distinct values ($\sim$150 combinations), with the A_i chosen in each case to reproduce the single-crystal spectra at g_1 and g_3 as well as the breadth of the pattern at g_2. As discussed immediately below, it was not possible to generate a peak that matches the behavior of 4A and also to reproduce the shift to low frequency of the doublet portion of the pattern. Therefore, we conclude that peak 4A is not related to the site B^1 doublet and that it represents the signal of a distinct iron site, labeled A^3, with negligible Larmor splitting and thus a negative hyperfine coupling.

Analysis of the resonances assigned to site B^1 was attempted by using collinear **A** and **g** tensors along with component values A_1 and A_2 that reproduce the single-crystal-like spectrum at g_1 and generate an acceptable breadth of intensity at g_2. These fail because the simulated pattern does not move sufficiently to low frequency as the field increases from g_1. This was worsened in simulations where the **A** tensor was rotated around the g_3 axis ($\alpha \neq 0$). As seen in Figure 7, simulations with the **A** tensor rotated around g_2 by $\beta = 45°$ and with the A_i values listed in Table I adequately reproduced the doublet that shifts sharply to low frequency with increasing field. This simulation also gives a peak that shifts concurrently to higher frequency, but which we assign as being unresolved in the experimental traces for the following reasons. In this simulation, with $A_3 = 10$ MHz, the B^1 doublet is well described, but the calculated additional peak is not at sufficiently high frequency, particularly in the spectra between $g = 4.14$ and 3.90 (Figure 7), to permit its assignment as peak 4A. Among numerous other simulations with $A_3 = 10$ MHz, none gave a peak that shifted even this far to high frequency yet reproduced the behavior of the doublet. When the alternate assignment of $A_3 = 19$ MHz is adopted and the remaining parameters are chosen to duplicate the behavior of the B^2 doublet, then the simulations display a peak that does match the shifts of peak 4A for low observing fields $g_1 > g \gtrsim g_2$. However, as the observing field is increased further, the experimental peak 4A shifts back to lower frequencies but the peak in the simulations does not. Instead, it continues to higher frequency as the observing g value is decreased; for $g \lesssim 3.5$ the predicted peak falls at frequencies where there are no peaks in the experimental spectra. Therefore, peak 4A is assigned to a separate iron site A^3, in which case the simulation of the B^1 doublet requires that the g_3 resonance of the B^1 site be assigned to the group with the lower hyperfine interaction, $A_3 \sim 10$ MHz.

Simulations for site A^3 were attempted with its A_1 and A_2 tensor components deduced from the resonance frequencies seen at g_1 and g_2, respectively, on the assumption of collinear **g** and **A** tensors. These did not reproduce the rapid shift to higher frequency with observing field evident in the experimental data for the intermediate fields $g_1 > g > g_2$. Therefore, simulations were performed over a grid in (α, β, γ) space, as described for site B^1. Rotation of the tensor about the g_2 ($\beta \neq 0$) axis did not solve the problem. However, simulations in which the hyperfine tensor is rotated about the g_3 axis ($\alpha = 30°$) and that utilize appropriate A_i values (Table I) reproduce the experimental pattern (Figure 7). A_3 was determined to be $\sim$−10 MHz because simulations with $A_3 \sim -20$ MHz give a peak at too high a frequency when $g < g_2$.

The B^2 doublet first shifts to lower frequency and then retreats to higher frequency as g is decreased from g_1 to g_2 (Figure 7). In addition, as the magnetic field increases, the proton pattern (centered at ν_H) moves to higher frequency and overlaps with the features from the B^2 site. Simulations of site B^2 with collinear **A** and **g** tensors and with A_1 and A_2 chosen appropriately could not reproduce the initial shift to lower frequency evident in the experimental spectrum taken at $g = 4.14$. Therefore, simulations were again performed over a grid of the Euler angles. The simulations in Figure 7, which used the **A** tensor listed in Table I and a rotation about the g_3 axis ($\alpha = 12°$), correlate well with the full set of experimental spectra. Although they include a low-frequency peak that is not evident in the experimental data, this absence is taken to be due to cross-relaxation from the proton resonances that fall in this range. Simulations with the further rotation $\beta \neq 0$ shifted the pattern too low in frequency.

The A_3 tensor component for site B^2 is tentatively assigned to be $\sim$20 MHz, because preliminary measurements[20] on the MoFe protein of the *nifV*$^-$ mutant of *K. pneumoniae* suggest a correlation between the B^2 doublet seen at g_y and the highest frequency iron doublet at g_3; the remaining low-frequency doublet at g_3 was assigned to site A^1. The experimental data do not rule out a value of $A_3 \sim 10$ MHz for site B^2 and a corresponding value of $A_3 \sim 19$ MHz for site A^1; this possibility represents the sole uncertainty in the assignments at g_3 and is indicated in Table I.

Other Iron Sites. Careful examination at fields near g_3 showed no additional resonances from ^{57}Fe. Also, in the low-field spectra taken near g_1 there are no unassigned, resolved features at frequencies above ca. 8 MHz. The Mössbauer results indicate there is another B site (or sites) with small positive coupling that should display ENDOR signals at low frequency.[3,21] However, we note that strong proton resonances observed at ca. 8 MHz for fields near g_1 with the natural-abundance Av1 are of greatly reduced intensity in the spectrum of a ^{57}Fe-enriched sample.[22] This suggests that the proton resonances overlap and cross-relax with the expected ^{57}Fe signal, making both resonances unobservable. ENDOR studies at higher field (spectrometer frequency) should clarify this issue.

Discussion

Mössbauer spectroscopic studies originally disclosed that the iron sites of the cofactor cluster of Av1 fall into two subclasses.[2,3] Three sites, labeled here as A^1–A^3, have relatively large, negative hyperfine coupling parameters. Another subclass, labeled B, and quantitated at three contributing sites, was found to have smaller, positive coupling constants. This observation first demonstrated unambiguously that the cofactor cluster is an antiferromagnetically spin-coupled structure.

The elegant Mössbauer analysis, carried out in the face of severe experimental difficulties and intrinsic limitations on the information derivable about hyperfine anisotropy, was forced to adopt the simplifying assumption of isotropic hyperfine interactions. In an unprecedented application of the ENDOR technique to frozen-solution samples, we have obtained anisotropic hyperfine tensor principal values *and* orientations relative to the zero-field splitting axes for five distinct iron sites, A^1–A^3, B^1, and B^2. The results obtained are summarized in Table I. The values for A_1 are specified ±0.1 MHz by the single-crystal-like spectra at g_1; those for A_2 are determined to within ±1 MHz by the field dependences. Values for the A_3 are quite accurately determined[8] by the spectra taken at g_3, but as discussed above, assignments of a value of A_3 to a particular site are at best binary, $A_3 \sim 10$ MHz or $A_3 \sim 19$ MHz. In general, the nonzero Euler angles for a particular ^{57}Fe tensor are specified to within ca. ±3° by the simulations. However, at least in some cases, the simulations may be relatively insensitive to other rotations over the range of fields that gives well-resolved spectra. For example, simulations for site A^1 demand

---

(20) McLean, P. A.; True, A. E.; Nelson, M. J.; Chapman, S.; Godfrey, M. R.; Teo, B. K.; Orme-Johnson, W. H.; Hoffman, B. M. *J. Am. Chem. Soc.* **1987**, *109*, 943–945.

(21) Chapman, S. K.; Papaefthymiou, V.; Munck, E.; Orme-Johnson, W. H., manuscript in preparation.

(22) Venters, R. A. Ph.D. Thesis, Northwestern University, 1985.

that $\alpha = 15 \pm 1°$, but permit $\beta = 0 \pm 10°$.

The most challenging task in our analysis was the assignment of peak 4A as representing an independent iron site, A^3, rather than a component of the spectrum of site B^1. However, this assignment not only is indicated by the ENDOR simulations, but is in agreement with the Mössbauer data, which disclosed the presence of a third site, A^3, having a large, negative hyperfine coupling.[3]

This analysis of multisite polycrystalline ENDOR signals is the first of its type, and therefore we are hesitant to state categorically that for no site is there another, widely different, parameter set that can equally well reproduce the spectra. Nevertheless, excepting only perhaps site B^2 whose resonances are partially obscured by proton signals, we feel this is unlikely: the full exploration of the space of Euler angles, as well as the richness of the features in the experimental spectra and the high degree with which they are reproduced by calculation, indicate that we have obtained a realistic picture of the ^{57}Fe hyperfine interactions. Moreover, since the simulations account for all of the features in the ENDOR spectra taken at numerous fields, we conclude that there are no other magnetically inequivalent iron sites with hyperfine coupling parameters as large as those listed in Table I.

Although present measurements improve the precision and detail obtainable from the analysis of the Mössbauer spectra from this cluster, it is gratifying and significant that the two techniques are in excellent agreement. The isotropic hyperfine coupling constant for each individual A site derived by Mössbauer spectroscopy[3] agrees well with the average of the hyperfine tensor compounds for that site as determined by ENDOR spectroscopy. The isotropic coupling constant for the B component of the Mössbauer spectra also is consistent with the averages of the B^1 and B^2 sites from ENDOR.

The most fundamental issue regarding the cofactor cluster, its composition, remains in dispute. The chemical analysis of isolated cofactor is compatible with 6–8 iron equivalents,[4] and the original Mössbauer quantitation,[3c] indicating that FeMo-co contains "approximately 5–7, most likely 6, Fe atoms", has been challenged and a suggestion made that there are 8 Fe.[23] The present ENDOR measurements directly observe five distinct Fe sites and thus set a lower limit consistent with the original Mössbauer quantitations. In the Mössbauer analysis,[3c] the B component of the Mössbauer spectrum of Av1, although unresolved and fit to a single coupling constant, was quantitated to three sites. The ENDOR spectra resolve two B sites. The intensity of an ENDOR pattern need not scale simply with the number of contributing nuclei, and thus either B^1 or B^2 might represent two equivalent sites. However, this would require both hyperfine tensor components and orientation to be the same. Considering the range in properties for the five distinct hyperfine tensors listed in Table I, an accidental equivalence would be remarkable, whereas equivalence by symmetry might suggest a functional significance.

We have noted above that it is unlikely that there are additional distinct sites whose hyperfine couplings at g_1 or g_2 are as large as those observed by ENDOR, and the Mössbauer quantitations rule out the possibility that an A-site resonance represents two or more magnetically equivalent Fe atoms. Thus, it seems that a sixth or seventh or eighth Fe atom, if present, must have small hyperfine coupling(s). We have discussed such a possibility; spectra taken at higher field (microwave frequency; e.g., 35 GHz) will resolve the issue.

The X-band ENDOR results presented here will play a further, powerful role in resolving the issue of composition when utilized in the quantitative analysis of Mössbauer spectra of the cluster. As noted above, Mössbauer measurements are unable to resolve the B sites or to determine the hyperfine tensor anisotropy for a center, such as FeMo-co, having a large spread in g values. The use of ENDOR-derived hyperfine tensors in performing a Mössbauer analysis gives a more realistic description of the iron sites, while simplifying the fitting procedure. Thus, the hyperfine tensors deduced by ENDOR spectroscopy form an important element in renewed efforts to use Mössbauer spectroscopy to determine the composition of the cofactors. Indeed, preliminary ENDOR results already have been so applied.[21]

The long-range goal in spectroscopic investigation of the cofactor is to elucidate the electronic properties of each individual metal site within the cluster as part of the basis for understanding the molecular mechanism of dinitrogen reduction. As judged from the fact that the Mössbauer spectra of the Av1 cofactor cluster[2b,19] can be interpreted in terms of a single quadrupole splitting, $|\Delta E_Q| = 0.76$ mm/s, for all sites, the iron environments of the cofactor would appear to be equivalent. This appearance is only somewhat dispelled by considering the isomer shifts: The three A sites have been assigned a slightly different isomer shift ($\gamma = 0.47$ mm/s) than B ($\gamma = 0.35$ mm/s). However, when the magnetic hyperfine parameters are examined, it becomes clear that the sites are remarkably different. The Mössbauer analysis showed that the average magnetic hyperfine interaction of an A-site nucleus is almost twice that of a B site and that the interactions are of opposite sign. The present ENDOR study even more dramatically suggests that the cofactor cluster has a remarkably complex structure: Five distinct Fe sites have been identified, no two of which have equivalent hyperfine tensor components or orientation.

To what extent is the structural complexity indicated by the site inequivalences intrinsic to the cluster, and not the result of distortions imposed by the protein environment on an intrinsically more symmetric form? EPR studies of the isolated cofactor suggest a degree of plasticity to its structure. The g values of FeMo-co as isolated with the Shah-Brill procedure[24] differ somewhat from those of Av1 and the EPR spectrum is broad, which suggests a distribution of conformations.[24] Moreover, a new preparative procedure has led to the observation that the EPR spectrum of FeMo-co in NMF solution depends on cluster concentration as well as on salt concentration.[21] Under appropriate conditions the g values are very close to those observed for the MoFe proteins. Mössbauer studies of such a sample give results in good agreement with the ENDOR measurements of Av1,[21] which strongly suggests that the structural complexity of FeMo-co bound at the active site of Av1 is intrinsic to the cluster, and not imposed by protein constraints.

Can valencies be assigned to the iron sites? The Mössbauer isomer shift and quadrupole splitting parameters demonstrate that the iron sites of the cofactor center do not exhibit trapped valences as seen in the $[Fe_2S_2]$ clusters of two-iron ferredoxins, but rather more closely approach the delocalized valences exhibited by the $[Fe_4S_4]$ cubes of four- and eight-iron ferredoxins and the high-potential iron–protein. The isomer shift for the A sites is intermediate between that observed for Fe(II) and Fe(III) tetrahedrally coordinated by sulfur; that for the B sites is somewhat closer to the values for Fe(III).[25]

The degree of anisotropy by the hyperfine coupling tensor of a high-spin iron site can provide a signature for its valency.[25] Typically, the ratio R of the smallest to largest components of the A tensor is about 0.5 or less for high-spin Fe(II), whereas the tensor for high-spin Fe(III) is roughly isotropic, with tensor components within 15% of their average value ($R \geq 0.75$). However, hyperfine anisotropy in a spin-coupled cluster also can arise as a consequence of the local zero-field splitting interactions associated with an individual site,[26] and thus it seems inappropriate to attempt firm assignments of valency at this time.

Summary

The cofactor cluster has a remarkably complex structure: no two of the five resolved Fe sites have equivalent hyperfine tensor components or orientation, and this low symmetry appears to be intrinsic, not imposed by the protein. It seems similarly intriguing

---

[23] Dunham, W. R.; Hagen, W. R.; Braaksma, A.; Grande, H. J.; Haaker, H. *Eur. J. Biochem.* **1985**, *146*, 497–501.

[24] Shah, V. K.; Brill, W. J. *Proc. Natl. Acad. Sci. U.S.A.* **1977**, *74*, 3247–3253.

[25] Huynh, B. H.; Kent, T. A. *Adv. Inorg. Biochem.* **1984**, *6*, 163–223.

[26] (a) Guiglarelli, B.; Gayda, J. P.; Bertand, P.; More, C. *Biochim. Biophys. Acta* **1986**, *871*, 149–155. (b) Munck, E., private communication.

that the magnetic properties of the metal sites are not homogenized by the strong electron delocalization demonstrated by the isomer shift and quadrupole splitting parameters.

Acknowledgment. This work was supported by Grants PCM 8350218 (B.M.H.) and PCM 8205764 (W.H.O.-J.) from the National Science Foundation Biophysics Program, and also by the donors of the Petroleum Research Fund, administered by the American Chemical Society (B.M.H.), and Grants 84-CRCR-1-1407 (W.H.O.-J.) and 87-CRCR-1-2430 (B.M.H.) from the USDA. The ENDOR spectrometer was purchased with a grant from the NSF Biological Instrumentation Program (PCM-8116106) and received support from Grant HL 13531 from the NIH (B.M.H.) and the Northwestern University Materials Research Center under the NSF—MRC Program (DMR 8216972).

Registry No. ^{57}Fe, 14762-69-7; nitrogenase MoFe cofactor, 72994-52-6.

Analysis of NMR and Absorption Spectroscopic Data in Bacteriorhodopsin: Models for Protein–Chromophore Interactions

Hillary S. Rodman Gilson and Barry H. Honig*

Contribution from the Department of Biochemistry and Molecular Biophysics, Columbia University, New York, New York 10032. Received October 27, 1986

Abstract: Detailed models for the interaction between the chromophore of bacteriorhodopsin and its protein environment are presented. The models are based on an analysis of the solid-state ^{13}C NMR data and the spectroscopic data derived from modified bacteriorhodopsin pigments in which the chromophore is replaced with a series of dihydroretinals. Semiempirical quantum mechanical methods are used to guide the analysis. The main features of the models include the following: a counterion whose electrostatic interaction with the Schiff base is weaker than that of a chloride counterion in solution; a negative charge near C5; a positive charge near C7; and a ring–chain conformation with a smaller torsional angle around the 6–7 single bond than is found in solution. Models with both s-cis and s-trans ring–chain conformations give excellent agreement with the absorption spectroscopic and chemical shift data. Although a number of recent experiments have led to the suggestion that an s-trans conformation is present in bR, arguments are presented that indicate that an s-cis ring–chain conformation cannot be ruled out.

Bacteriorhodopsin (bR) belongs to a group of biological pigments (retinal proteins) that use a protonated Schiff base of retinal as a chromophore. Although all of the pigments in this group contain retinal as a chromophore, both their absorption maxima (λ_{max}) and their biological function can be quite different. Thus, it is the arrangement of amino acids in each protein that both regulates the spectral properties of the chromophore and determines how the energy of the absorbed photon is to be used. In the absence of high-resolution three-dimensional structures of these pigments, a variety of spectroscopic techniques have been used to study the interactions between the protein and the chromophore.

Models for wavelength-determining interactions in the retinal binding site of bR have been based on both absorption spectra and solid-state NMR data. The essential absorption measurements were carried out on bR and on modified bR's in which the chromophore was replaced with a series of dihydroretinals (see Table I).$^{1-3}$ The NMR results were obtained in the series of experiments of Harbison et al., who succeeded in measuring the ^{13}C and ^{15}N chemical shifts of the retinal chromophore of bR.$^{4-8}$

Table I. Calculated and Experimental λ_{max} (nm) of PRSB and bR and Opsin Shifts (OS) (cm^{-1})

chromophore	all-trans	5,6-H_2	7,8-H_2	9,10-H_2
PRSB^a	445	431	392^b	322
(calcd)^a	448	435	392	336^c
bR^a	567	478	440	
OS	4830	2340	2780	
(calcd)	571	480	437	
OS	4800	2160	2630	
bR^d	568	475	445	

^{a} Data taken from Spudich et al.^{2}. ^{b} Nakanishi et al.^{1} and Lugtenburg et al.^{3} reported a value of 385 nm for the λ_{max} of 7,8-dihydro-PRSB. We reproduced this λ_{max} using a C=N syn conformation in our calculations. It is thus possible that the discrepancy in the data is a result of different configurations about the C=N bond. ^{c} The 322-nm λ_{max} is reproduced when a C=N syn conformation is used in our calculations (see above). ^{d} Data from Lugtenburg et al.^{3}

The major qualitative features of the models proposed to account for the 570-nm absorption maximum of bR include (1) a weak counterion–Schiff base interaction, (2) an s-trans conformation about the C6–C7 single bond (the ring–chain angle) rather than the s-cis conformation that is the energetically favored form in solution,^{9} and (3) a negative charge near C5 that forms an ion pair with a positive charge near C7. Quantum mechanical calculations of absorption maxima were used to derive a model for chromophore–protein interactions in which the location of the charged groups on the protein was explicitly defined. However, the interpretation of the NMR data was based entirely on qualitative arguments. In this paper the NMR data are also

---

(1) Nakanishi, K.; Balogh-Nair, V.; Arnaboldi, M.; Tsujimoto, K.; Honig, B. *J. Am. Chem. Soc.* **1980**, *102*, 7945–7947.

(2) Spudich, J. L.; McCain, D. A.; Nakanishi, K.; Okabe, M.; Shimizu, N.; Rodman, H.; Honig, B.; Bogomolni, R. A. *Biophys. J.* **1986**, *49*, 479–483.

(3) Lugtenburg, J.; Muradin-Szweykowska, M.; Heeremans, C.; Pardoen, J. A.; Harbison, G. S.; Herzfeld, J.; Griffin, R. G.; Smith, S. O.; Mathies, R. A. *J. Am. Chem. Soc.* **1986**, *10*,, 3104–3105.

(4) Harbison, G. S.; Herzfeld, J.; Griffin, R. G. *Biochemistry* **1983**, *22*, 1–5.

(5) Harbison, G. S.; Smith, S. O.; Pardoen, J. A.; Winkel, C.; Lugtenburg, J.; Herzfeld, J.; Mathies, R.; Griffin, R. G. *Proc. Natl. Acad. Sci. U.S.A.* **1984**, *81*, 1706–1709.

(6) Harbison, G. S.; Smith, S. O.; Pardoen, J. A.; Mulder, P. P. J.; Lugtenburg, J.; Herzfeld, J.; Mathies, R.; Griffin, R. G. *Biochemistry* **1984**, *23*, 2662–2667.

(7) Harbison, G. S.; Mulder, P. P. J.; Herzfeld, J.; Griffin, R. G. *J. Am. Chem. Soc.* **1985**, *107*, 4809–4819.

(8) Harbison, G. S.; Smith, S. O.; Pardoen, J. A.; Courtin, J. M. L.; Lugtenburg, J.; Herzfeld, J.; Mathies, R. A.; Griffin, R. G. *Biochemistry* **1985**, *24*, 6955–6962.

(9) Honig, G.; Warshel, A.; Karplus, M. *Acc. Chem. Res.* **1975**, *8*, 92–100.